AIAA 2003-0066

ON LARGE EDDY SIMULATION OF HIGH REYNOLDS NUMBER WALL-BOUNDED FLOWS

Christer Fureby
The Swedish Defence Research Agency, FOI
Dept. of Weapons & Protection, SE-172 90 Stockholm, Sweden
Lund Institute of Technology
Dept. of Fluid Mechanics, SE-221 00 Lund, Sweden

Niklas Alin, Niklas Wikström
The Swedish Defence Research Agency, FOI
Dept. of Weapons & Protection, SE-172 90 Stockholm, Sweden

Nils Svanstedt
Chalmers University of Technology, SE-412 96 Göteborg, Sweden

Suresh Menon
Georgia Institute of Technology,
School of Aerospace Engineering, Atlanta, GA, 30332-0150, USA

Leif Persson
The Swedish Defence Research Agency, FOI,
Dept. of NBC Defence, SE-901 82 Umeå, Sweden

41th AIAA Aerospace Sciences Meeting & Exhibit
6-9 January 2003 / Reno, NV

ON LARGE EDDY SIMULATION OF HIGH REYNOLDS NUMBER WALL BOUNDED FLOWS

C. Fureby[a,b], N. Alin[a], N. Wikström[a], N. Svanstedt[c], S. Menon[d] & L. Persson[e]
[a] The Swedish Defence Research Agency, FOI, Dept. of Weapons and Protection,
Warheads and Propulsion, SE-172 90 Stockholm, Sweden
[b] Lund Institute of Technology, Dept. of Fluid Mechanics
SE-221 00 Lund, Sweden
[c] Dept. of Mathematics,
Chalmers University of Technology, SE-412 96 Göteborg, Sweden
[d] Georgia Institute of Technology,
School of Aerospace Engineering, Atlanta, GA, 30332-0150, USA
[e] The Swedish Defence Research Agency, FOI, Dept. of NBC Defence
Environment and Protection, SE-901 82 Umeå, Sweden

Abstract

Large Eddy Simulation (LES) of wall-bounded flows becomes prohibitively expensive at high Reynolds (Re) numbers if one attempts to resolve the small but dynamically important vortical structures in the near-wall region. The LES wall-boundary condition problem is thus to account for the effects of the near-wall turbulence between the wall and the first node and its transfer of momentum to the wall. Here we state the problem and give a brief overview of methods currently in use, and possible future methods. To illustrate the problem and quantify the accuracy of some of the models we present a few results from test cases ranging from fully developed turbulent channel flows to three-dimensional problems of practical engineering interest.

1. Introduction

Almost all practical flows are turbulent and hence the simulation of turbulent flow and its diversity of flow characteristics remains one of the most challenging areas in the field of classical physics. Most Computational Fluid Dynamic (CFD) codes presently used for high Reynolds (Re) number complex flows are based on the well-known Reynolds Average Navier-Stokes (RANS) equations, [1-2], together with a turbulence model, [2-4], for representing the effects of turbulence on the mean flow. Although RANS correctly predicts the mean flow in many cases, RANS often fail when facing more complex flows. Moreover, RANS is not appropriate when unsteady flow features are of primary concern or when these dominate the flow. On the other hand, Direct Numerical Simulation (DNS), in which all scales are resolved, is currently too expensive to be used for practical problems.

Large Eddy Simulations (LES), [4-9], present an alternative way of improving qualitative and quantitative aspects of complex turbulent flow predictions for both research and engineering purposes. LES resolves the three-dimensional time-dependent details of the large and medium (i.e. resolved) scales, whereas the effects of the small unresolved eddies are modelled with a subgrid turbulence model. The separation into grid and subgrid scales is usually accomplished by a low-pass filter tied to the grid, but other methods are now also slowly coming into use, cf. [10]. Despite three decades of intensive research, and yet unresolved issues, LES is considered the most promising method for studying complex flows. Although it will remain expensive in terms of cpu time and memory LES can be the only reliable method for simulating complex flows where RANS is inadequate.

Wall-bounded flows are characterized by much less universal properties than free flows (ideally considered homogeneous isotropic) and are therefore more challenging to compute. Within the viscous sublayer the characteristic length scale is determined by the friction velocity u_τ and the viscosity ν, and outside of this, the length scale of the most energetic eddies can scale as the distance from the wall. As Re increases, and the thickness of the viscous sublayer decreases, the number of grid points required to resolve the near-wall flow structures increases. Bagget *et al*, [11], estimated that the number of grid points required for a 'wall-resolved LES' scales as $\mathcal{O}(\mathrm{Re}_\tau^2)$, where Re_τ is the friction velocity based Re-number. Moreover, unless the grid is sufficiently fine, the anisotropy of the flow will cause anisotropy of the subgrid flow, necessitating subgrid models capable of handling simultaneous flow and grid anisotropy. Consequently, high

Re-number flows, especially in complex geometries, are too expensive to compute with LES unless particular techniques are invoked to alleviate the severe resolution requirements near the wall.

In principle this can be achieved by following either of the following approaches:

- modify the subgrid model to accommodate integration all the way to the wall, taking simultaneous flow and grid anisotropy into account,
- use separate wall-models,
- use subgrid simulation models, which are based on e.g. multi-scales techniques.

In this paper we will try to summarize these methods and give a few illustrative examples to expose the features of these methods.

The outline of this paper is as follows: In sections 2 and 3 we give a brief outline of conventional and alternative LES models whereas in sections 4 and 5 we present two novel LES methods based on multi-scales techniques, suited for wall-bounded flows. In Sections 6, 7 and 8 we give a few examples of applications and in section 9 we conclude.

2. Large Eddy Simulation

Here we outline the classical LES formulation, give a few examples of alternative formulations and finish with a discussion of the near-wall complication.

2.1. Mathematical Formulation

In LES the flow variables are decomposed into large-scale components (denoted by overbars) and small-scale (subgrid) components (denoted by primes) by applying a filtering operation,

$$\bar{f}(\mathbf{x},t)=G*f(\mathbf{x},t)=\int_D G(\mathbf{x}-\mathbf{z},\Delta)f(\mathbf{z},t)d^3\mathbf{z}, \tag{1}$$

where G is the filter function and Δ the filter width. Applying the filtering operation to the NSE yields,

$$\begin{cases}\nabla\cdot\bar{\mathbf{v}}=m^\rho,\\ \partial_t(\bar{\mathbf{v}})+\nabla\cdot(\bar{\mathbf{v}}\otimes\bar{\mathbf{v}})=-\nabla\bar{p}+\nabla\cdot\bar{\mathbf{S}}-\nabla\cdot\mathbf{B}+\mathbf{m}^\nu,\end{cases} \tag{2}$$

where $\bar{\mathbf{v}}$ is the velocity, $\bar{p}$ the pressure, $\bar{\mathbf{S}}=2\nu\bar{\mathbf{D}}$ the viscous stress tensor, $\bar{\mathbf{D}}=\frac{1}{2}(\bar{\mathbf{L}}+\bar{\mathbf{L}}^T)$ the rate-of-strain tensor, $\bar{\mathbf{L}}=\nabla\bar{\mathbf{v}}$ the velocity gradient tensor, and ν the viscosity. Specific to the LES model (2) are the subgrid stress tensor $\mathbf{B}=\overline{\mathbf{v}\otimes\mathbf{v}}-\bar{\mathbf{v}}\otimes\bar{\mathbf{v}}$ and the commutation errors are $\mathbf{m}^\nu=[G*,\nabla](\mathbf{v}\otimes\mathbf{v}+p\mathbf{I}-\mathbf{S})$ and $m^\rho=[G*,\nabla]\mathbf{v}$, where $[G*,\nabla]f=\overline{\nabla f}-\nabla\bar{f}$ is the commutation operator, [12-13]. Only the resolved scales are thus retained in LES whereas the subgrid scale flow physics is grouped into **B**, which has to be modelled using a functional expression of the type $\mathbf{B}(\mathbf{x},t)=\mathbf{B}[\bar{\mathbf{v}}(\mathbf{x}',t');\mathbf{x},t]$. Physical arguments and mathematical analysis, e.g. [13-15], suggest that: (i) **B** is invariant under a change of frame; (ii) **B** is positive definite symmetric, provided that $G(\mathbf{x},\Delta)$ is symmetric; and (iii) that the inequalities $k=\frac{1}{2}\mathrm{tr}\mathbf{B}\geq 0$, $k^2\geq\|\mathbf{B}\|^2$ and $\det\mathbf{B}\geq 0$ must be satisfied for **B** to be positive definite. Furthermore, the commutation error terms, m^ρ and $\mathbf{m}^\nu$, reflect the fact that filtering and differentiation do not generally commute, [13, 16]. The effects of m^ρ and $\mathbf{m}^\nu$ on the resolved flow are not yet fully understood and must be further examined, [16], and in the meantime, these terms are usually grouped into the subgrid stress tensor **B** that is subject to modelling.

2.2. Subgrid Modelling

We usually separate between *Functional modelling*, which consists of modelling the action of the subgrid scales on the resolved scales, and *Structural modelling*, which consists of modelling the subgrid stresses without incorporating any knowledge about the interactions between the subgrid and the resolved scales, [6]. However, for the purpose of this paper we prefer to instead separate between *isotropic* and *anisotropic* subgrid models since high Re-number complex flows often are characterized by anisotropic flow on a wide range of scales – typically reaching into the range of scales that require modelling, as e.g. in the near-wall region. The most frequently used subgrid models belong to the first category, viz.,

$$\mathbf{B}_D=\mathbf{B}-\tfrac{2}{3}k\mathbf{I}=-2\nu_k\bar{\mathbf{D}},\quad k=\tfrac{1}{2}\mathrm{tr}\mathbf{B}, \tag{3}$$

where ν_k is the (scalar) subgrid eddy-viscosity. To close (3) we need models for the eddy-viscosity ν_k and the turbulent kinetic energy k, and for this we assume the existence of characteristic length and velocity scales and we infer separation between resolved and subgrid scales. Among these we have the One-Equation-Eddy-Viscosity Model (OEEVM), [17],

$$\begin{aligned}&\partial_t(k)+\nabla\cdot(k\mathbf{v})=2\nu_k\|\bar{\mathbf{D}}\|^2+\nabla\cdot((\nu+\nu_k)\nabla k)+c_\varepsilon\frac{k^{3/2}}{\Delta},\\ &\nu_k=c_k\Delta k^{1/2},\end{aligned} \tag{4}$$

and the Smagorinsky (SMG) model, [18],

$$k=c_I\Delta^2\|\bar{\mathbf{D}}\|^2,\ \nu_k=c_D\Delta^2\|\bar{\mathbf{D}}\|, \tag{5}$$

where the model coefficients (c_I, c_D, c_k and c_ε) are evaluated either from a $|\mathbf{k}|^{-5/3}$ inertial sub-range behavior resulting in constant coefficients, or from a dynamic procedure, producing spatio-temporally varying coefficients. Different dynamic calculation methods have been suggested, e.g. the dynamic Smagorinsky Model (DSMG), [19], the One-Equation Dynamic Localization Model, (DLM), [20], the Localized Dynamic Kinetic Energy Model (LDKM), [21-23], as well as the Lagrangian Dynamic Model (LDM), [24].

For anisotropic flows, with anisotropy extending into the subgrid scales, more advanced subgrid models are required. Structural models are superior (at least from a theoretical standpoint) to functional models in such flows since they do not rely on the local isotropy assumptions on which the functional models are based. The best examples of structural models are the Mixed Model (MM) of Bardina *et al.*, [25],

$$\mathbf{B}=\overline{\overline{\mathbf{v}}\otimes\overline{\mathbf{v}}}-\overline{\overline{\mathbf{v}}}\otimes\overline{\overline{\mathbf{v}}}-2\nu_k\overline{\mathbf{D}}, \tag{6}$$

and the Differential Stress Equation Model (DSEM), Deardorff, [26]. The DSEM uses a modelled transport equation for the subgrid stress tensor **B**,

$$\begin{aligned}\partial_t(\mathbf{B})+\nabla\cdot(\mathbf{B}\otimes\overline{\mathbf{v}})=&-(\overline{\mathbf{L}}\overline{\mathbf{B}}^{\mathrm{T}}+\mathbf{B}\overline{\mathbf{L}}^{\mathrm{T}})\\&+\nabla\cdot(\nu_k\nabla\mathbf{B})-c_m\tfrac{k^{1/2}}{\Delta}\mathbf{B}_D+\tfrac{2}{5}k\overline{\mathbf{D}}_D+(\tfrac{2}{3}c_m-c_\varepsilon)\tfrac{k^{3/2}}{\Delta}\mathbf{I},\end{aligned} \tag{7}$$

where $\nu_k=c_k\Delta k^{1/2}$ and $k=\frac{1}{2}\mathrm{tr}\mathbf{B}$. The model coefficients are estimated from isotropic turbulence, and take the values $c_m=4.13$, $c_k=0.07$ and $c_\varepsilon=1.35$. Anisotropic functional models have been developed by Carati & Cabot, [27], and Abba *et al.*, [28], using fourth-rank tensor eddy-viscosities, by Horiuti, [29], using multilevel filtering, and by Schumann, [17], and Sullivan *et al*, [30], using a decomposition of **B** into isotropic and anisotropic components.

2.3. Near-Wall Flow Physics and Modeling

Close to a solid wall, to the leading order in y, being the distance from the wall, the resolvable velocity $\overline{\mathbf{v}}$ can be expanded in a Taylor series of the form,

$$\overline{\mathbf{v}}=(\overline{b}_1y)\mathbf{e}_1+(\overline{c}_2y^2)\mathbf{e}_2+(\overline{b}_3y)\mathbf{e}_3, \tag{8}$$

where $\mathbf{e}_i$, i=1,2,3, are unit vectors in the streamwise, wall-normal and spanwise directions, and b_1, c_2 and b_3 are random functions. Similarly for B_{ij},

$$B_{ij}=\begin{bmatrix}(\overline{b_1^2}-\overline{b}_1^{\,2})y^2 & (\overline{b_1c_2}-\overline{b}_1\overline{c}_2)y^3 & (\overline{b_3c_2}-\overline{b}_3\overline{c}_2)y^2\\ & (\overline{c_2^2}-\overline{c}_2^{\,2})y^4 & (\overline{b_3c_2}-\overline{b}_3\overline{c}_2)y^3\\ \text{sym} & & (\overline{b_3^2}-\overline{b}_3^{\,2})y^2\end{bmatrix}. \tag{9}$$

The LES model is thus required to satisfy not only the boundary condition $\overline{\mathbf{v}}=\mathbf{0}$ but also the conditions (9) on **B** when $y\to0$. Considering the SMG model, (3)-(5), we have that $\partial\overline{v}_1/\partial x_2=\overline{b}_1$ and $\partial\overline{v}_3/\partial x_2=\overline{b}_3$ so that $B_{12}=-c_D\Delta^2(\overline{b}_1^2+\overline{b}_3^2)^{1/2}\overline{b}_1$ and unless $\Delta\propto y^{3/2}$ incorrect asymptotic behaviour at the wall is obtained. For example, if (3) is to be used, a necessary requirement is that $k\propto y^2$ and $\nu_k\propto y^3$, when $y\to0$, in order for **B** to comply with (9). Most structural models satisfy (9) automatically but many models must be modified to satisfy (9). This can be done using:

- Damping functions, $\mathcal{D}$, that act as regularization prefactors to ν_k, such that $\nu_k=\mathcal{D}\nu_k$. Typically $\mathcal{D}=(1-\exp(-(\beta y^+)^3))^{1/2}$, where $y^+=u_\tau y/\nu$ is the viscous length scale, $u_\tau=\tau_w^{1/2}$ the friction velocity, τ_w the wall shear stress and $\overline{v}_i^+=\overline{v}_i/u_\tau$ a non-dimensionalized velocity component;
- Dynamic modelling based on Germanos identity, $\mathbf{L}=\mathbf{T}-\tilde{\mathbf{B}}$, [19-23], in which $\mathbf{L}=\overline{\overline{\mathbf{v}}\otimes\overline{\mathbf{v}}}-\overline{\overline{\mathbf{v}}}\otimes\overline{\overline{\mathbf{v}}}$ and $\mathbf{T}=\overline{\overline{\mathbf{v}}\otimes\overline{\mathbf{v}}}-\overline{\overline{\mathbf{v}}}\otimes\overline{\overline{\mathbf{v}}}$. By assuming that **B** and **T** can be closed with models of the same functional form i.e. $\mathbf{B}=-2c_D\Delta^2\|\overline{\mathbf{D}}\|\overline{\mathbf{D}}$ and $\mathbf{T}=-2c_D\overline{\Delta}^2\|\overline{\mathbf{D}}\|\overline{\mathbf{D}}$ we have that $\mathbf{L}_D=c_D\mathbf{X}-\overline{c_D\mathbf{Y}}$, where $\mathbf{X}=-2\Delta^2\|\overline{\mathbf{D}}\|\overline{\mathbf{D}}$ and $\mathbf{Y}=-2\overline{\Delta}^2\|\overline{\overline{\mathbf{D}}}\|\overline{\overline{\mathbf{D}}}$. Hence, in the least-squares sence $c_D=\mathbf{M}\cdot\mathbf{L}/\mathbf{M}\cdot\mathbf{M}$, where $\mathbf{M}=\mathbf{X}-\overline{\mathbf{Y}}$.
- Dynamic modelling based on the self-similarity between B and $\mathbf{L}=\overline{\overline{\mathbf{v}}\otimes\overline{\mathbf{v}}}-\overline{\overline{\mathbf{v}}}\otimes\overline{\overline{\mathbf{v}}}$, [24]. This observation can be used to evaluate the coefficient c_k and c_ε in the OEEVM (4). Bounds for c_k and c_ε are determined from the realizabilty constraints.
- Models for the eddy-viscosity coefficients that include viscous effects, cf. [31]. If the model coefficients (c_D and c_k) are derived from more elaborate versions of the energy spectrum than the inertial subrange spectrum $E=K_0\varepsilon^{2/3}|\mathbf{k}|^{-5/3}$, e.g. the Pao spectrum $E=\exp(-\frac{3}{2}K_0(|\mathbf{k}|\lambda_K)^{4/3})$, it is found that these coefficients are not constants but complicated functions of the mesh Re-number $\mathrm{Re}_\Delta=\Delta^2\|\overline{\mathbf{D}}\|/\nu$. This can be interpreted as models with scale-dependent coefficients and improves the predictive capabilities for transitional and wall-bounded flows.

Alternatively we may use wall models. The simplest wall models are based on analytical expressions for the wall shear stress, τ_w, and they provide an algebraic relationship between the local wall stresses and the tangential velocities at the first off-wall nodes. Such algebraic models all imply the logarithmic law of the wall for the mean velocity, which is not generally valid in complex flows. The equations governing for the wall-layer can be approximated by the boundary layer equations,

$$\partial_y(\nu(\partial_y\overline{v}_i)-B_{iy})=g_i;\ g_i=\partial_i\overline{p}+\partial_t\overline{v}_i+\partial_j(\overline{v}_i\overline{v}_j)-f_i, \tag{10}$$

[4]. Assuming that $g_i=0$ the stress $\nu(\partial_y\overline{v}_i)-B_{12}$ is independent of y, and since $B_{iy}=0$ on the wall (10) can be integrated analytically to give the law-of-the-wall,

$$\overline{v}^+=\begin{cases}y^+ & \text{if } y^+\le y_0^+,\\ \frac{1}{\kappa}\ln|y^+|+B & \text{if } y^+>y_0^+,\end{cases}\quad y_0^+\approx11.225, \tag{11}$$

where $\kappa\approx0.41$ is the von-Karmán constant and $B\approx5.2$. If $g_i=\partial_i\overline{p}$ it is still possible to integrate (10) analytically to recover the modified law-of-the-wall,

$$\overline{v}^+=\begin{cases} y^+ + \frac{y^+}{2u_\tau^2}\partial_i\overline{p} & \text{if } y^+ \le y_0^+(u_\tau,\partial_i\overline{p}), \\ \frac{1}{\kappa}\ln y^+ + \frac{y^+}{\kappa u_\tau^2}\partial_i\overline{p}+B & \text{if } y^+ > y_0^+(u_\tau,\partial_i\overline{p}). \end{cases} \quad (12)$$

For the full case, $g_i=\partial_i\overline{p}+\partial_t\overline{v}_i+\partial_j(\overline{v}_i\overline{v}_j)-f_i$, equation (10) has to be solved numerically. This approach has sucessfully been used by Wang, [32] and by Wang & Moin, [33], in which (10) is solved on an embedded near-wall grid to determine τ_w, using a mixing length model. Alternatively, (11) or (12) can used to modify the subgrid model by adding a subgrid wall-viscosity ν_{BC} to the viscosity ν on the wall so that the effective viscosity, $\nu+\nu_{BC}$, becomes,

$$\nu+\nu_{BC}=\tau_w/(\partial v_y/\partial y)_P=u_\tau y_{y,P}/v_{y,P}^+, \quad (13)$$

where the superscript P denotes that the quantity is to be evaluated at the first grid point away from the wall. This model can, in principle, be combined with any other subgrid model, and in the notation +WM is added to the baseline subgrid model name.

3. Alternative LES Models

As an alternative to model ν_k using k, as working variable as in (4), we may instead model ν_k by its own transport equation. The most well-known transport equation model for ν_k is probably that of Spalart-Allmaras, [34], in which $\nu_k=f_{v1}\tilde{\nu}$, where,

$$\begin{aligned}\partial_t(\tilde{\nu})+\nabla\cdot(\tilde{\nu}\mathbf{v})&=c_{b1}\tilde{S}\tilde{\nu}+\nabla\cdot([(\nu+\tilde{\nu})/\sigma]\nabla\tilde{\nu}) \\ &\quad +(c_{b2}/\sigma)(\nabla\tilde{\nu})^2-c_{w1}f_w(\tilde{\nu}/\tilde{d})^2,\end{aligned} \quad (14)$$

where $f_{v1}=\chi^3/(\chi^3+c_{v1}^3)$, $\chi=\tilde{\nu}/\nu$, $\tilde{D}=|\overline{\mathbf{D}}|+\tilde{\nu}f_{v2}/\kappa^2\tilde{d}^2$, $r=\tilde{\nu}/\tilde{D}\kappa^2\tilde{d}^2$, $f_{v2}=1-\chi/(1+\chi f_{v1})$, $g=r+c_{w2}(r^6-r)$, $f_w=g[(1+c_{w3}^6)/(g^6+c_{w3}^6)]^{1/6}$ and $\tilde{d}=\min(y,c_{DES}\Delta)$. The model coefficients are calibrated in simple homogeneous and free flows and take the values: $c_{b1}=0.135$, $c_{b2}=0.62$, $\sigma=2/3$, $\kappa=0.41$, $c_{w1}=3.24$, $c_{w2}=0.3$, $c_{w3}=2.0$, $c_{v1}=7.10$ and $c_{DES}=0.65$. This approach is commonly referred to as Detatched Eddy Simulation (DES), [35-36], but may be interpreted as LES.

In Monotone Integrated LES (MILES) the discretization effectively filters the NSE across the grid using an anisotropic kernel. When founding MILES on concepts like the Flux Corrected Transport (FCT), [37], the functional reconstruction of the convective fluxes is done using a flux-limiting method combining a high-order flux-function with a low-order dispersion-free flux-function using a non-linear flux-limiter Γ. Moreover, the functional reconstruction of the viscous fluxes is typically performed using linear interpolation. Similar approaches have been used by several authors, e.g. [38-42], and are discussed in greater deatail in [10], and references therein. Physical considerations motivating MILES have been presented in [42], and some formal properties were recently documented using databases of free and wall-bounded flows, [43]. The modified equations provide the most suitable platform for comparing MILES and LES and following [42] the implicit subgrid model is,

$$\mathbf{B}=\mathbf{C}\mathbf{L}^T+\mathbf{L}\mathbf{C}^T+\beta^2\mathbf{L}\mathbf{d}\otimes\mathbf{L}\mathbf{d},\ \mathbf{C}=\beta(\mathbf{v}\otimes\mathbf{d}), \quad (15)$$

where $\mathbf{d}$ is the inter-cell distance and $\beta=\beta(\Gamma)$. Because of the tensorial nature of the subgrid viscosity MILES offers an attractive alternative to conventional subgrid models when seeking improved LES for inhomogeneous flows.

4. The Two-Level Simulation LES Model

In the Two-Level Simulation (TLS) approach of Kemenov & Menon, [44-45], both the resolved and subgrid scales of motion are explicitly simulated. Regardless of how this approach is implemented it is clear that if both the resolved and subgrid scales are simulated in three-dimensions this method is no different from DNS, and thus far too expensive for engineering flow problems. However, insprired by Kerstein, [46], Kemenov & Menon developed an approach in which the large scales evolve on an ordinary LES-grid under the action of the subgrid force ($\nabla\cdot\mathbf{B}$) which is computed locally from the definition of the subgrid stress tensor $\mathbf{B}$ involving both large and small scales. The small scales evolve on locally embedded one-dimensional grids. This reduction in dimensionality permits the TLS approach to be computationally feasible and applicable to high Re-number flows.

In this framework the equations for the large scales are identical to the LES equations (2),

$$\begin{cases}\nabla\cdot\overline{\mathbf{v}}=0, \\ \partial_t(\overline{\mathbf{v}})+\nabla\cdot(\overline{\mathbf{v}}\otimes\overline{\mathbf{v}})=-\nabla\overline{p}+\nabla\cdot\overline{\mathbf{S}}-\nabla\cdot\mathbf{B},\end{cases} \quad (16)$$

whereas the equations for the small scales are,

$$\begin{cases}\nabla\cdot\mathbf{v}'=0, \\ \partial_t(\mathbf{v}')+\nabla\cdot(\mathbf{v}'\otimes\mathbf{v}')=-\nabla p'+\nabla\cdot(\nu\nabla\mathbf{v}') \\ \qquad +\nabla\cdot(\mathbf{B}-\overline{\mathbf{v}}\otimes\mathbf{v}'-\mathbf{v}'\otimes\overline{\mathbf{v}}),\end{cases} \quad (17)$$

where $\mathbf{B}=(\overline{\overline{\mathbf{v}}\otimes\overline{\mathbf{v}}}-\overline{\mathbf{v}}\otimes\overline{\mathbf{v}})+(\overline{\overline{\mathbf{v}}\otimes\mathbf{v}'}+\overline{\mathbf{v}'\otimes\overline{\mathbf{v}}})+(\overline{\mathbf{v}'\otimes\mathbf{v}'})$. In the TLS model (17) is simplified such that $\mathbf{v}'$ is modeled as a family of one-dimensional vector fields defined on lines of arbitrary orientation. When the orientation coincides with the orientation of the LES grid the resulting (one-dimensional) equations become particularly simple, cf. [44-45]. After that the equations for $\mathbf{v}'$ have been solved $\mathbf{B}$ can be obtained directly from its definition in each LES cell.

5. The Homogenization-Based LES Model

With the intent of deriving improved subgrid models, particularly for high Re-number wall-bounded flows, Persson *et al.*, [47], use homogenization by multiple-scales expansion, [48], to derive the LES model. To this end they introduce the two-scale expansion,

$$\begin{cases} \mathbf{v}=\mathbf{v}_\delta+\mathbf{v}'_\delta=\bar{\mathbf{v}}(\mathbf{x},t)+\sum_{k=1}^{\infty}\delta^k\mathbf{v}_k(\mathbf{x},t;\boldsymbol{\xi},\tau)+\mathbf{v}'_\delta(\boldsymbol{\xi},\tau), \\ p=\delta^{-2}p_{-2}+\delta^{-1}p_{-1}+\bar{p}+\tilde{p}+\sum_{k=1}^{\infty}\delta^k p_k(\mathbf{x},t;\boldsymbol{\xi},\tau), \end{cases} \tag{18}$$

where $\bar{\mathbf{v}}(\mathbf{x},t)=\mathbf{v}_0(\mathbf{x},t)$ and $\bar{p}=\bar{p}(\mathbf{x},t)$ denote the LES variables whereas $\tilde{p}=\tilde{p}(\boldsymbol{\xi},\tau)$ is the Lagrange multiplier necessary to guarantee that $\nabla_\xi\cdot\mathbf{v}_1=0$. For high Re not all eddy scales can be expected to be resolved, and hence $\mathbf{v}'_\delta$ is represented by a stochastic process $\mathbf{w}=\mathbf{w}(\boldsymbol{\xi},\tau)$ such that $\mathbf{v}'_\delta=\delta^{-1}\mathbf{v}_{-1}=\delta^{-1}\mathbf{w}(\boldsymbol{\xi},\tau)$. Here, $\boldsymbol{\xi}$ and τ denote the subgrid (or independent) variables. From the scaling symmetries of the NSE the only natural choise for the subgrid variables is $\tau=t/\delta^2$ and $\boldsymbol{\xi}=\mathbf{x}/\delta$. Formal expansion of the NSE using (16) and the chain rule of differentiation yields,

$$\begin{cases} \delta^{-2}\left[\nabla_\xi\cdot\mathbf{w}\right]+\delta^{-1}\left[\nabla\cdot\mathbf{w}\right]+\delta^{0}\left[\nabla\cdot\bar{\mathbf{v}}+\nabla_\xi\cdot\mathbf{v}_1\right] \\ \quad+\sum_{k=1}^{\infty}\delta^k\left[\nabla\cdot\mathbf{v}_k+\nabla_\xi\cdot\mathbf{v}_{k+1}\right]=0, \\ \delta^{-3}\left[\partial_\tau\mathbf{w}-\nu\nabla_\xi^2\mathbf{w}+\nabla_\xi\cdot(\mathbf{w}\otimes\mathbf{w})+\nabla_\xi p_{-2}\right] \\ \quad+\delta^{-2}\left[\nabla_x p_{-2}+\nabla_\xi p_{-1}\right] \\ \quad+\delta^{-1}\left[\nabla_x\cdot(\mathbf{w}\otimes\bar{\mathbf{v}})+\nabla_x p_{-1}+\partial_\tau\mathbf{v}_1-\nu\nabla_\xi^2\mathbf{v}_1\right. \\ \quad\left.+\nabla_\xi\cdot(\mathbf{w}\otimes\mathbf{v}_1+\mathbf{v}_1\otimes\mathbf{w})+\nabla_\xi\tilde{p}\right] \\ \quad+\delta^{0}\left[\partial_t\bar{\mathbf{v}}-\nu\nabla_x^2\bar{\mathbf{v}}+\nabla_x\cdot(\mathbf{w}\otimes\mathbf{v}_1+\bar{\mathbf{v}}\otimes\bar{\mathbf{v}}+\mathbf{v}_1\otimes\mathbf{w})\right. \\ \quad-2\nu(\nabla_\xi\cdot\nabla_x)\mathbf{v}_1+\nabla_x\bar{p}+\partial_\tau\mathbf{v}_2-\nu\nabla_\xi^2\mathbf{v}_2 \\ \quad\left.+\nabla_\xi\cdot(\mathbf{w}\otimes\mathbf{v}_2+\mathbf{v}_2\otimes\mathbf{w})+\nabla_\xi p_1\right] \\ \quad+\sum_{k=1}^{\infty}\delta^k\left[\partial_t\mathbf{v}_k-\nu\nabla_x^2\mathbf{v}_k-2\nu(\nabla_\xi\cdot\nabla_x)\mathbf{v}_{k+1}\right. \\ \quad+\nabla_x p_k+\partial_\tau\mathbf{v}_{k+2}+\nabla_x\cdot(\mathbf{w}\otimes\mathbf{v}_{k+1}+\bar{\mathbf{v}}\otimes\mathbf{v}_k \\ \quad+\sum_{j=1}^{k-1}[\mathbf{v}_j\otimes\mathbf{v}_{k-j}]+\mathbf{v}_k\otimes\bar{\mathbf{v}}+\mathbf{v}_{k+1}\otimes\mathbf{w})-\nu\nabla_\xi^2\mathbf{v}_{k+2} \\ \quad+\nabla_\xi\cdot(\mathbf{w}\otimes\mathbf{v}_{k+2}+\sum_{j=1}^{k}[\mathbf{v}_j\otimes\mathbf{v}_{k+1-j}]+\mathbf{v}_{k+1}\otimes\bar{\mathbf{v}} \\ \quad\left.+\mathbf{v}_{k+2}\otimes\mathbf{w})+\nabla_\xi p_{k+1}\right]=\mathbf{f}. \end{cases} \tag{19}$$

where ∂_t and ∇_x, and ∂_τ and ∇_ξ denote differentiation with respect to supergrid and subgrid variables. Averaging (19) over $\boldsymbol{\xi}$ and τ and identifying coefficients for δ^{-1} gives the LES equations,

$$\begin{cases} \nabla_x\cdot\bar{\mathbf{v}}=0, \\ \partial_t\bar{\mathbf{v}}+\nabla_x\cdot(\bar{\mathbf{v}}\otimes\bar{\mathbf{v}})=-\nabla_x\bar{p}+\nabla_x\cdot(\nu\nabla_x\bar{\mathbf{v}}-\mathbf{B})+\mathbf{f}, \end{cases} \tag{20}$$

where $\mathbf{B}=\overline{\mathbf{w}\otimes\mathbf{v}_1}+\overline{\mathbf{v}_1\otimes\mathbf{w}}$ is the subgrid stress tensor. In order to close (20) we need to supply $\mathbf{w}$ and $\mathbf{v}_1$. Identification of coefficients for δ^{-3} in equation (20) yields that $p_{-2}=p_{-2}(\boldsymbol{\xi},\tau)$ and that the stochastic process $\mathbf{w}$ must obey $\partial_\tau\mathbf{w}+\nabla_\xi\cdot(\mathbf{w}\otimes\mathbf{w})=\nu\nabla_\xi^2\mathbf{w}-\nabla_\xi p_{-2}$, with zero mean over each LES cell. Identifying coefficients for δ^{-2} in (20) now shows that $p_{-1}=0$. Finally, identification of coefficients for δ^{-1} in (20) results in the subgrid (or microstructure) problem,

$$\begin{cases} \nabla_\xi\cdot\mathbf{v}_1=0, \\ \partial_\tau\mathbf{v}_1+\nabla_\xi\cdot(\mathbf{w}\otimes\mathbf{v}_1+\mathbf{v}_1\otimes\mathbf{w})=-\nabla_\xi\tilde{p}+\nu\nabla_\xi^2\mathbf{v}_1 \\ \qquad\qquad -\nabla_x\cdot(\mathbf{w}\otimes\bar{\mathbf{v}}), \end{cases} \tag{21}$$

and from which (together with $\mathbf{w}$) the subgrid stress tensor $\mathbf{B}=\overline{\mathbf{w}\otimes\mathbf{v}_1}+\overline{\mathbf{v}_1\otimes\mathbf{w}}$ can be obtained.

The fact that $\mathbf{v}_1$ depends only parametrically on $\nabla_x\bar{\mathbf{v}}$ allowed Persson *et al.*, [47], to derive solutions to (21) by superposition from problems without parameter dependence, satisfying,

$$\begin{cases} \partial_{\xi^m}\chi^m_{kl}=0, \\ \partial_\tau\chi^j_{kl}+\partial_{\xi^m}(w^m\chi^j_{kl}+\chi^m_{kl}w^j)=\nu\nabla^2_\xi\chi^j_{kl}-\delta^j_k w^l, \end{cases} \tag{22}$$

so that $v_1^j=\chi^j_{kl}\partial_{x^l}\bar{v}^\kappa$, from which it is evident that,

$$B_{ij}=\overline{(w^i\chi^j_{kl}+w^j\chi^i_{kl})}\partial_{x^l}\bar{v}^k=A_{ijkl}\partial_{x^l}\bar{v}^k, \tag{23}$$

where A_{ijkl} is a fourth-rank eddy-viscosity tensor. In [47] an attempt was made to estimate A_{ijkl} based on a particular choise of $\mathbf{w}$ and the assumption of negligible subgrid transport. The choice of $\mathbf{w}$ is not simple, but chosing $\mathbf{w}$ to comply with the Kolmogorov inertial subrange spectrum $E(\mathbf{k})=c_K\varepsilon^{2/3}\mathbf{k}^{-5/3}$ and to satisfy the constrain $\nabla\cdot\mathbf{w}=0$ yields that,

$$A_{hjkl}=\frac{c_K c_\varepsilon^{2/3}k\Delta^2}{(2\pi)^{11/3}\nu}\tilde{A}_{hjkl}, \tag{24}$$

where $A_{hjkl}=A_{hjkl}(\boldsymbol{\Delta})$ is a tensor expressing the local anisotropic grid scaling.

6. Numerics

The application of LES to engineering problems requires not only good subgrid models and fast computers, but also accurate and robust numerical methods. Unstructured grids are desirable since the time required for generating unstructured grids is usually considerably lower than for block-structured grids. To this end the Finite Volume (FV) method is appropriate. However, non-dissipative schemes that conserve not only momentum but also kinetic energy are required for successful LES computations. Discrete conservation of kinetic energy ensures robustness without numerical dissipation, which compromises accuray.

In the FV-method, the domain D is partitioned into non-overlapping cells Ω_P. The cell-average of the field f over the P^{th} cell is $f_P=\frac{1}{\delta V}\int_\Omega f dV$ so that Gauss theorem may be used to formulate the semi-discretized LES-equations. By integrating these in time, using e.g. a multi-step method, [49], the discretized LES-

equations ((2) and (18)) become,

$$\begin{cases} \frac{\beta_i \Delta t}{\delta V_P}\sum_f [F_f^{C,\rho}]^{n+i}=0, \\ \sum_{i=0}^{m}(\alpha_i(\bar{\mathbf{v}})_P^{n+i}+\frac{\beta_i \Delta t}{\delta V_P}\sum_f[\mathbf{F}_f^{C,v}+\mathbf{F}_f^{D,v}]^{n+i}) \\ \qquad =-\beta_i(\nabla \bar{p})_P^{n+i}\Delta t+\beta_i \bar{\mathbf{f}}_P^{n+i}\Delta t, \end{cases} \tag{25}$$

where m, α_i and β_i are parameters of the scheme and $F_f^{C,\rho}=(\bar{\mathbf{v}}\cdot d\mathbf{A})_f$, $\mathbf{F}_f^{C,v}=(\bar{\mathbf{v}}\cdot d\mathbf{A})_f\,\bar{\mathbf{v}}_f$, $\mathbf{F}_f^{D,v}=(\nu\nabla\bar{\mathbf{v}}-\mathbf{B})_f\,d\mathbf{A}$ are the convective and viscous fluxes. In order to obtain 2nd order accuracy, a cell-centered scheme is used, utilizing linear interpolation for the convective fluxes and central difference approximations for the gradients in the viscous fluxes. Conservation of kinetic energy is automatically satisfied. Time-integration is carried out by a three-point scheme defined by m=2, $\alpha_0=1/2$, $\alpha_1=-2$, $\alpha_2=3/2$, $\beta_0=\beta_1=0$ and $\beta_2=1$, and hence,

$$\begin{cases} a_P(\bar{\mathbf{v}})_P^{n+2}=\mathbf{H}(\bar{\mathbf{v}})-(\nabla\bar{p})_P^{n+2}+(\bar{\mathbf{f}})_P^{n+2}, \\ \mathbf{H}(\bar{\mathbf{v}})=\sum_N a_N(\bar{\mathbf{v}})_N^{n+2}+\frac{1}{2\Delta t}(\bar{\mathbf{v}})_P^{n}-\frac{2}{\Delta t}(\bar{\mathbf{v}})_P^{n+1}, \end{cases} \tag{26}$$

where the coefficients a_P and a_N are functions of the dependent variables. By combining (25_1) and (25_2), we obtain the Poisson equation,

$$\nabla\cdot(a_P^{-1}(\nabla\bar{p})^{n+2})=\sum_f(a_P^{-1}[\mathbf{H}(\bar{\mathbf{v}})+(\bar{\mathbf{f}})_P^{n+2}])_f\cdot d\mathbf{A} \tag{27}$$

where the Laplace operator is discretized in a standard manner and $F_f^{C,\rho}$ is evaluated from the interpolated velocity field $\bar{\mathbf{v}}_f^{n+2}=(a_P^{-1}[H(\bar{\mathbf{v}})-(\nabla\bar{p})_P^{n+2}+\bar{\mathbf{f}}_P^{n+2}])_f$. The scalar equations are usually solved sequentially, with iteration over the explicit source terms to obtain rapid convergence, with the additional requirement that the Courant number Co<0.4.

While tetrahedral cells allow complex geometries to be easily meshed, they are not well suited for turbulent flows – our experience shows that hexahedral cells are preferable since they give more accurate solutions. The grid may therefore be a combination of arbitrary polyhedral cells, with mainly hexahedral cells but using e.g. tetrahedral cells in regions that are difficult to mesh with hexahedral cells.

7. Turbulent Channel Flow

The first test case to be discussed is a fully developed turbulent channel flow at (bulk) Re-numbers between 15,000 and 800,000. The channel is confined between two perfectly smooth parallel plates 2h apart, where h is the channel half-width. The flow is driven by a fixed mass flow in the streamwise ($\mathbf{e}_x$) direction defining the mean velocity $\langle\bar{\mathbf{v}}\rangle$. No-slip conditions are used in the cross-stream ($\mathbf{e}_y$) direction and periodic conditions are used in the spanwise ($\mathbf{e}_z$) direction. As initial conditions a parabolic velocity distribution is used. After reaching a statistically steady state the runs were continued for another $40\cdot h/u_\tau$ time-units to collect appropriate statistics. The friction velocity is $u_\tau=\tau_w^{1/2}$ and τ_w is the wall-shear stress. The size of the channel is 6h×2h×3h in the streamwise, cross-stream and spanwise directions, respectively. Instead of varying the grid we vary the mass flow to obtain three target Re-numbers: Re_τ=395, 2030 and 10,000, of which the first correspond to the DNS data, [50-51], and the second to the experimental data, [52]. The grid consists of 60^3 cells with uniform spacing in the stream- and spanwise directions whereas geometrical progression is used in the $\mathbf{e}_y$ direction to cluster the grid towards the walls. Runs and nominal parameters are collected in Tables 1 and 2, respectively.

Table 1. *Channel flow grids.*

Re	Δx_1^+	$min(\Delta x_2^+)$	Δx_3^+
395	40	0.3	20
2030	200	2	100
10,000	1000	11	500

Table 2. *Nominal parameters of the channel flow runs*

Run	*Re*	*Grid*	*Subgrid model*	C_f
Dean [53]	395		—	0.00655
I	403	60^3	OEEVM	0.00648
II	402		OEEVM+WM	0.00653
III	399		LDKM	0.00654
IV	405		MILES	0.0065
V	404		DES	0.0061
VI	404		HOM	0.00647
Dean [53]	2030			0.00435
VII	2036	60^3	OEEVM	0.00421
VIII	2046		OEEVM+WM	0.00439
IX	2049		LDKM	0.00436
X	2021		MILES	0.0433
XI	2054		DES	0.0423
Dean [53]	10000			0.00253
XII	10087	60^3	OEEVM	0.00212
XIII	10076		OEEVM+WM	0.00238
XIV	10054		LDKM	0.00244
XV	10065		MILES	0.00259
XVI	10034		DES	0.00261

Figure 1 shows the main flow features of the channel flow in terms of vortex lines, contours of $\bar{v}_x$ and iso-surfaces of the second invariant of the velocity gradient $Q=\frac{1}{2}(\|\mathbf{W}\|^2-\|\mathbf{D}\|^2)$. The location of a vortex line is given by the equation $d\mathbf{x}/ds=\bar{\boldsymbol{\omega}}/|\bar{\boldsymbol{\omega}}|$, where s is the distance along the vortex line. This equation is integrated using a 3rd order Runge-Kutta method together with a 2nd order linear interpolation scheme to compute $\bar{\boldsymbol{\omega}}$ from the grid points. By correlating iso-surfaces of Q with $\bar{\mathbf{v}}$ close to the wall it is found that vortices above the low-speed streaks are often ejected away from the wall, as found in experiments and LES and DNS, producing hairpin vortices stretched by the ambient shear. By this mechansim vorticity produced in the viscous region is advected into the boundary layer, making it turbulent. As in DNS and other LES the hairpin vortices are often asymmetric – with one

leg stronger than the other. The spanwise resolution is found more important for the accurate prediction of the coherent structure dynamics than the streamwise resolution. The wall-normal resolution is critical for the correct prediction of τ_w, which, in turn, is important for making correct estimates of the drag.

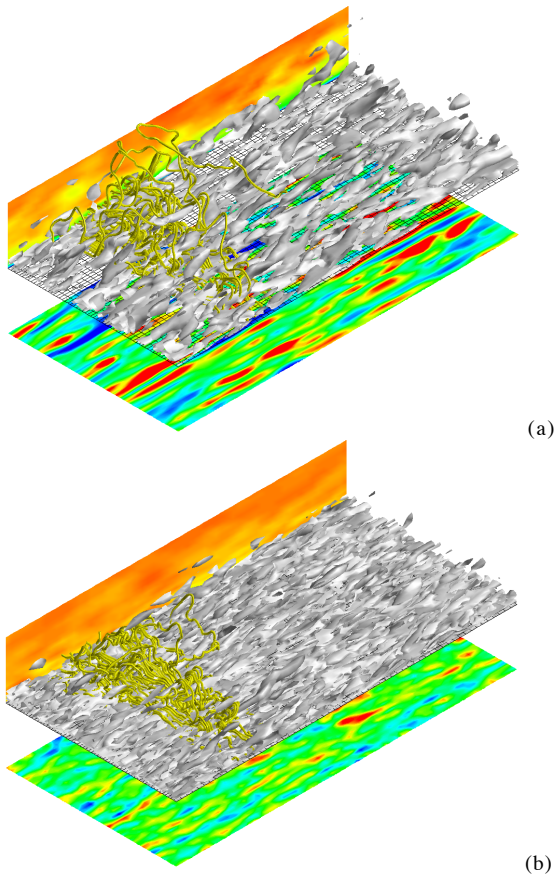

Figure 1. Perspectives of fully developed turbulent channel flow simulations at (a) Re_τ=395 and (b) Re_τ=10000. Both datasets presented are obtained with the LDKM.

In figure 2 we compare our LES predictions of the time-averaged streamwise velocity $\langle \overline{v}_x \rangle$ (integrated over x and z) with the DNS data, [50], experimental data, [52], and analytical expressions. In figure 2a we plot $\langle \overline{v}_x \rangle / u_\tau$ against y/h from the wall, whereas in figure 2b we plot $\langle \overline{v}_x \rangle / u_\tau$ against $y^+ = y u_\tau / \nu$. For R_τ=395 all LES models examined (cf. Table 2) show excellent agreement with the DNS data across the entire channel. The integrated difference along the cross-stream coordinate, y, is smaller than 2% of the bulk velocity for any model. Hence, when the flow is very well resolved the details of the subgrid model are of little importance to the resolved flow, since most of the energy (about 98%) and structures are resolved on the grid. For R_τ=2030 we still see good agreement between LES and experimental data, but with somewhat larger scatter in the LES data. This case is reasonably well resolved, with about 90% of the energy belonging to the resolved scales. For R_τ=10,000 we do not have any data to compare with, but we may compare (asymptotically) with the lower Re_τ-number velocity profiles and the log-law. The scatter among the LES models is now larger, and we find the best agreement between the log-law and the LES results for DES and LDKM followed, in turn, by MILES, OEEVM+WM and OEEVM. The DES model is successful since the Spalart-Allmares model works well for zero pressure-gradient boundary-layers, [35]. The LDKM is successful since ν_k responds to the accumulation of energy in the small scales by adjusting the dissipation before it contaminates the resolved scales. MILES performs since it mimics the anisotropies of the resolved flow, [42]. OEEVM+WM works since the channel flow is dominated by two zero-pressure gradient boundary layers, for which the wall model is tailor-made, but the OEEVM appears unable to capture the near-wall boundary layer very well.

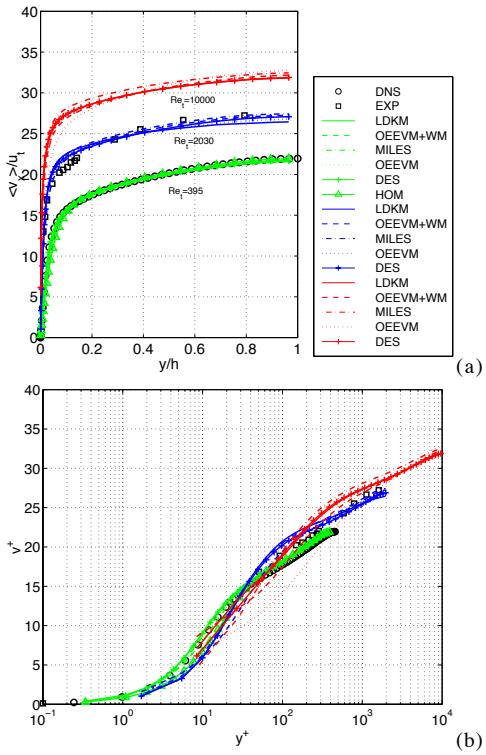

Figure 2. Time-averaged streamwise velocity profiles. (a) in linear scaling and (b) in logarithmic scaling for fully developed turbulent channel flows at Re_τ=395, 2030 and 10,000.

In figure 3 we compare LES predictions of the resolved kinetic energy $k = \frac{1}{2}\langle \overline{v}_i'^2 \rangle$, where $\overline{\mathbf{v}}' = \overline{\mathbf{v}} - \langle \overline{\mathbf{v}} \rangle$ are the velocity fluctuations, (integrated over x and z) with experimental data, [50], DNS data, [52]. For R_τ=395 very good agreement with the DNS results is obtained across the entire channel for any LES model. For R_τ=2030 the agreement between LES and data is only fair; best agreement is obtained with the LDKM and worst agreement is obtained with the DES model. The trend is that the predicted profiles are wider than the measured profiles, and that the LES models cannot capture the peak in k, at about $y^+ \approx 15$, but over-

predicts it by about 15%. For R_τ=10,000 the scatter between the LES predictions is wider.

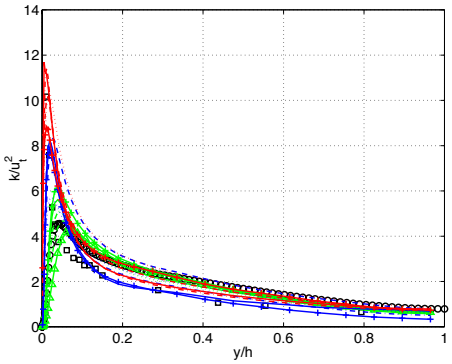

Figure 3. Turbulent kinetic energy, k, profiles for fully developed turbulent channel flows at Re_τ=395, 2030 and 10,000.

In figure 4 we compare LES predictions of the resolvable (Reynolds) shear stress $\bar{R}_{xy}=\langle \bar{v}'_x \bar{v}'_y \rangle$, with experimental data, [50], and DNS data, [52], for the total shear stress $R_{xy}=\langle v'_x v'_y \rangle$. Both R_{xy}-profiles are bounded by the line $R_{xy}=u_\tau^2 y/h$, which constitute an upper bound for R_{xy}. For R_τ=395 excellent agreement with the DNS results is obtained between 0.3<y/h<1, and between 0<y/h<0.3 $\bar{R}_{xy}<R_{xy}$, as a consequence of the action of the subgrid model, that covers almost 80% of this difference. For R_τ=2030 and R_τ=10,000 similar results are observed, but since R_{xy} is expected to follow $R_{xy}=u_\tau^2 y/h$ asymptotically with increasing Re_τ-number, the fraction of the shear stress to be covered by the subgrid model is increasing, thus putting larger demands on the subgrid model. The only exception from the general behaviour is the DES model, which however gives good predictions for other quantities examined. At present we do not know the cause of these anomalities.

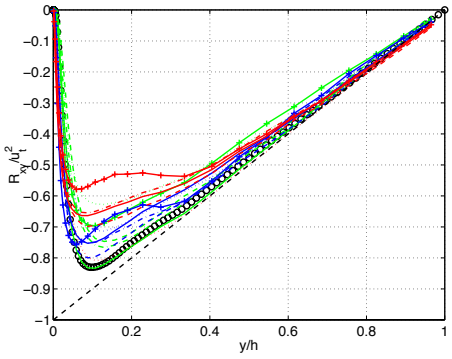

Figure 4. Reynolds shear stress, R_{xy}, profiles for fully developed turbulent channel flows at Re_τ=395, 2030 and 10,000.

Comparing statistics from the LES with the correlations of Dean, [53], $U_C/U_m \approx 1.28 \cdot Re_m^{-0.016}$ and $C_f \approx 0.073 \cdot Re_m^{-0.25}$, where U_C is the mean centerline velocity and $Re_m=U_m 2\delta/\nu$, shows good agreement at Re_τ=395, but at Re_τ=2030 and 10,000 this agreement declines. In general, however LDKM, DES and MILES give best agreement. This is related to the resolution; at Re_τ=395 the mean streak-spacing is well-resolved, whereas for the remaining Re_τ it is not. For Re_τ=2030 and 10,000 the mean streak-spacing seems to be related to the spanwise resolution.

8. Flow over an Axisymmetric Hill

In our attempts to extend the use of LES to engineering problems of practical interest a particularly interesting issue is that of flows over curved surfaces. In [54] LES, using the LDKM, of the flow over an axisymmetric hill have been conducted and is compared to measurements of Simpson *et al,* [55].

According to the investigations of Simpson *et al,* [56], these flows produce complex vortical structures with multiple separation and re-attachment zones covering a large part of the lee-side of the hill. It is also observed that geometrically similar hills (of hill-height H=2δ and H=δ) yield qualitatively and quantitatively different flow dynamics. Hence, the flow past such objects is very complicated. It is not yet fully understood as to why a small change in the geometry configuration results in a flow pattern that shows little or no resemblance to the original one.

Figure 5 presents the geometry. The axisymmetric hill-height H is 0.078 m with the circular base of radius R=2H. The zenith of the hill is about 3.4H downstream from the inflow boundary and the computational domain extends 6H in the spanwise direction. The shape of the hill is defined analytically by,

$$y(r)=\frac{H}{6.04844}[J_0(\Lambda)I_0(\Lambda r/R)-I_0(\Lambda)J_0(\Lambda r/R)], \qquad (28)$$

where Λ=3.1926, J_0 is the Bessel function of the first kind and I_0 is the modified Bessel function of the first kind. The Re-number, based on H and the flow velocity (v_0=27.5 m/s), is about $1.3 \cdot 10^5$. A structured but stretched grid of 256×128×128 cells is used, in which the minimum grid spacing in the wall-normal direction is approximately $\Delta y^+ \approx 4$. This resolution is chosen so as to give us enough grid points near the surface to reasonably resolve the boundary layer and the separation downstream of the hill.

Figure 5. Schematic of the computational domain.

Simpson *et al.*, [55], report profiles with the speed v_0 and with 0.1% freestream turbulence intensity, having a boundary layer thickness of $\delta_{99} \approx 39$mm, and $Re_\theta \approx 7300$. Similar inflow profiles were used, in which a Gaussian random field (0.1% of the mean) is added to the inlet velocity profile in order to emulate the freestream turbulence. To wash out the effects of

the initial conditions the simulations are allowed to evolve several flow-through-times before any data is collected for analysis.

Figure 6 presents a comparison of the predicted surface streamline pattern (colored by velocity magnitude) with the experimental oil flow pattern. We observe complex flow patterns on the lee-side of the hill with multiple recirculation regions. Complex vortical structures appear just downstream of the zenith of the hill, where also multiple separations can be seen. Initially, these structures have some coherence upstream of the hill but later, these structures break down into small-scale structures. The velocity (not shown) suggests separation on the lee-side that re-attaches and separates. A similar multi-stage separation and reattachment has been seen in experiments, [56].

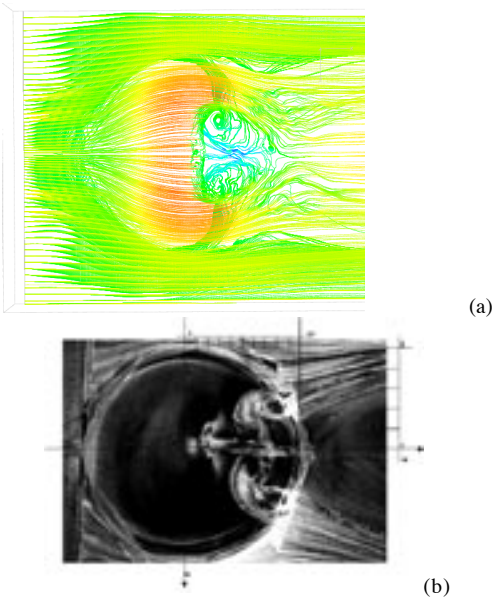

(a)

(b)

Figure 6. Oil-flow visualizations (using streamlines colored by the velocoty in the near-wall regions) for the numerical study (a) and the experiments (b).

Typical results for the (time-averaged) static pressure coefficient $C_P=(\bar{p}-p_0)/(\tilde{p}-p_0)$, where $\bar{p}$ is the local static pressure, p_0 is the static reference pressure and $\tilde{p}$ is the local total pressure are presented and compared with the experimental measurement data in figure 7. We find that LES predict the principal trends observed experimentally. However, there are a few differences in the contour patterns on the lee-side of the hill where the vortical separations are observed. The contour patterns remain symmetric about the hill center plane upstream of separation zone.

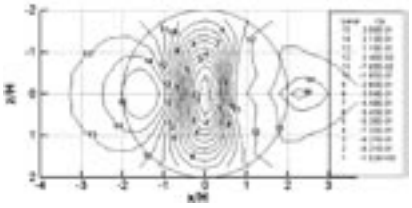

(a)

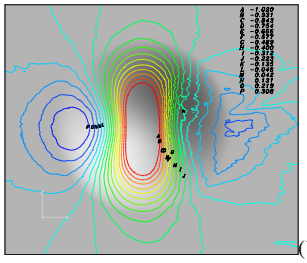

(b)

Figure 7. Measured (a) and predicted (b) static pressure coefficients C_P contours over the hill surface.

Figure 8 presents comparisons for the streamwise velocity, normalized by the fricton velocity u_t, at a streamwise location of 3.69H downstream of the hill peak for various spanwise locations on either side of the center plane. The agreement between LES, using LDKM, and the experimental data is qualitatively and quantitatively good. In particular, we notice that the LES capture the detailed variation of the velocity in the spanwise direction, which is considered promising considering the complexity of the flow.

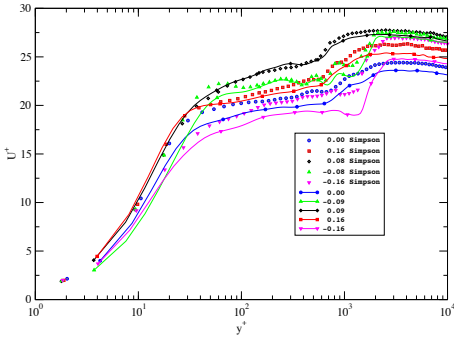

Figure 8. Comparison of the predicted and measured velocity profiles at 3.69H downstream of the hill peak for various spanwise locations on either side of the center plane

9. Flow over an Inclined Prolate Spheroid

Despite its simple geometry, the flow around a manœuvring prolate spheroid, or a prolate spheroid at an incidence, figure 9, contains a rich gallery of complex three-dimensional flow features. These include stagnation flow, three-dimensional boundary layers under influence of pressure gradients and streamline curvature, cross-flow separation and the formation of free vortex sheets ensuing streamwise vortices. These features are archetypes of flows around airborne and underwater vehicles warranting an in-depth study.

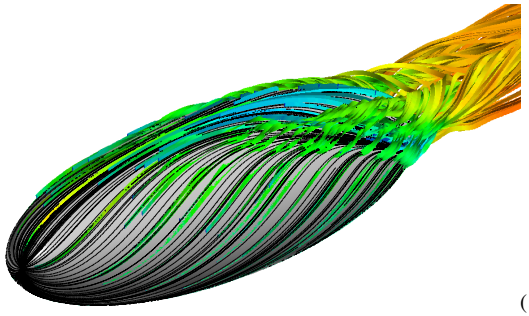

(a)

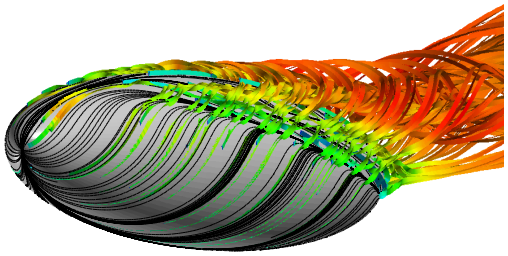

(b)

Figure 9. Perspective view of the cross-flow separation and the associated longitudinal vortices on a 6:1 prolate spheroid at (a) α=10° and (b) α=20°, respectively.

Here and in [57-58] we consider the flow around a 6:1 prolate spheroid, mounted in a wind-tunnel with rectangular cross-section, [59-66]. The body length is L=1.37 m and the tunnel cross-section is 1.8×1.8 m^2. The freestream velocity is v_0=46 m/s creating a body-length Re-number of $Re_L=4.2\cdot10^6$. Detailed measurements have been carried out at angles-of-attack between α=0° and α=30°, [59-65], and here we focus on α=10° and 20°. Contrary to the study of Hedin *et al.*, [58], and for the simulations to be compared to those of Constantinescu *et al.*, [67], the computational domain consists of a sphere with radius R=2L. This has the advantage of simplifying gridding, thus producing grids of high quality with modest stretching, warpage and skewness. The disadvantage is that the blocking effects are neglected, but these are generally considered small in comparison to neglecting the supporting sting on which the body is mounted and the effects of the freestream wind-tunnel specific flow.

The grid topology consists of two blocks: an inner O-grid that wraps around the body, and an outer O-grid that fills the region between the inner grid and the outer spherical boundary. In [59-65], two grids of about $0.8\cdot10^6$ and $1.6\cdot10^6$ cells are used. These grids have average wall-normal distances of $y^+\approx20$ and 30, respectively, and a radial stretching ratio (for the inner O-grid) of 1.10. At the inlet, $\bar{\mathbf{v}}=v_0\mathbf{n}$ and $\partial\bar{p}/\partial\mathbf{n}=\mathbf{0}$, where $\mathbf{n}$ is the outward pointing unit normal, and at the outlet $\bar{p}=p_\infty$ and $\partial(\bar{\mathbf{v}}\cdot\mathbf{n})/\partial\mathbf{n}=\mathbf{0}$. On the body, no-slip conditions are utilized. After the initial transients vanish, the statistical sampling was started, and sufficient time (25,000 time steps) is allowed for each of the runs to develop time-averaged data for the first and second order statistical moments of $\bar{p}$ and $\bar{\mathbf{v}}$. Table 3 summarizes the results reported here.

Table 3. Prolate spheroid simulations.

run	*grid*	α	*subgrid model*
I	$0.8\cdot10^6$	10	OEEVM+WM
II	$0.8\cdot10^6$	20	OEEVM
III	$0.8\cdot10^6$	20	LDKM
IV	$0.8\cdot10^6$	20	OEEVM+WM
V	$1.6\cdot10^6$	20	OEEVM+WM

In figure 10 we present the static pressure coefficient $C_P=2(\langle p\rangle-p_0)/v_0^2$, where p_0 is a reference pressure, in the meridian plane. For α=10° the agreement between LES and experimental data is generally good, especially on the leeward side. On the windward side, in the aft region, there is some discrepancy, possibly related to the presence of the support sting used in the experiments but not included in the LES'. For α=20° no experimental data exists, but good agreement is found between the different LES'. In figure 10b, C_P is shown as function of φ (the azimuthal angle measured from the symmetry plane on the windward side of the body) at x/L=0.772. For α=10° the agreement between LES and experimental data is good with the exception of the sector between φ=120° and 150°. This corresponds to the region beneath the primary vortex, cf. figure 9, and from theoretical considerations we expect a low-pressure patch on the hull beneath that vortex. For α=20°, C_P shows the existence of both a primary and a secondary separation on the body and the agreement between experimental data and LES is good, especially on the windward side.

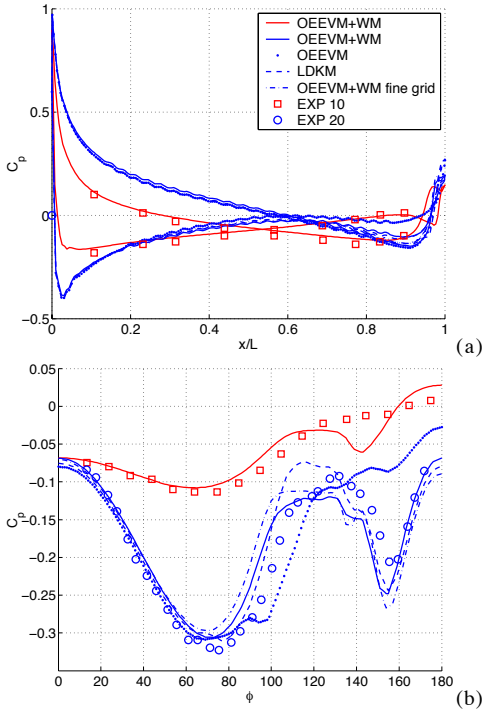

Figure 10. Comparison of the static pressure coefficient, C_P, at (a) the meridian plane and (b) x/L=0.772.

Figure 11 shows the normalized time-averaged, velocity components (U,V,W) in the body coordinate system along two lines orthogonal to the body originating at x/L=0.6, φ=90°, and x/L=0.772, φ=90°, for α=10° and α=20°, respectively. Here, U is tangent to the body pointing towards the tail, V is normal to the body (positive outwards) whereas W is orthogonal to both U and V. For both angles-of-attack the LDKM and the OEEVM+WM give good agreement between predictions and experiments. OEEVM overpredicts U and W in the outer part of the boundary layer at x/L=0.6 and underpredicts U and W in the entire boundary

layer at x/L=0.772. This is likely to be caused by insufficient resolution of the inner part of the boundary layer, which is taken care of by the wall-model in the OEEVM+WM. Increasing the wall-normal resolution with the OEEVM supports this, whereas increasing the resolution in the volume with the OEEVM+WM does not alter the profiles significantly.

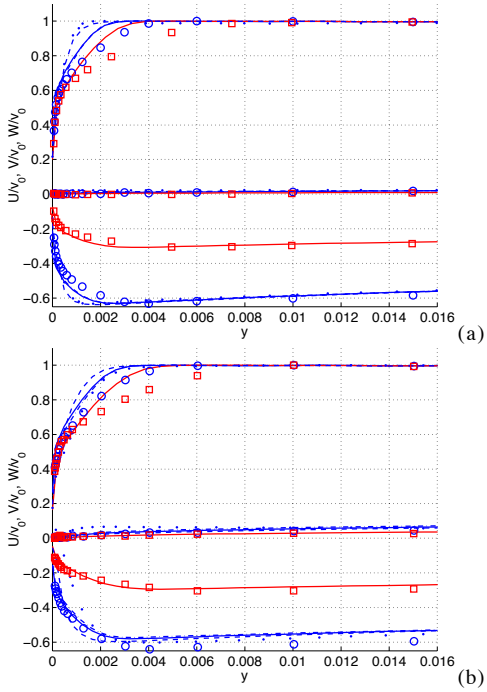

Figure 11. Comparison of the normalized velocity (U, V, W) in the body surface coordinate system at (a) x/L=0.6, φ=90° and (b) x/L=0.772, φ=90°. Note that the results and data for the α=10° case are shifted one unit in the ordinate direction. For legend see figure 10.

Figures 12 and 13 show secondary streamlines superimposed on gray-scale contours of the resolvable turbulent kinetic energy $k=\frac{1}{2}\langle(\overline{\mathbf{v}}-\langle\overline{\mathbf{v}}\rangle)^2\rangle^{1/2}$ (left) and on U (right) In figure 12 we present results from the OEEVM, and in figure 13 we show results from the LDKM. For α=10° and x/L=0.6 neither experiments nor LES show true vortices (defined by closed streamlines), but instead a sheet of fluid rolling-up. At x/L=0.772 both experiments and LES show true vortices at around φ≈145° and about 1.3 cm above the body surface. For α=20° and x/L=0.6 the primary vortex is at φ≈152° and 2.2 cm above the body surface for the OEEVM, whereas for the LDKM it is at φ≈150° and 1.9 cm above the body surface. At x/L=0.772 the primary vortex is at φ≈152° and 3.0 cm above the body surface for the OEEVM, whereas for the LDKM it is at φ≈153° and 3.3 cm above the body surface. For α=20° a secondary vortex is found close to the body at φ≈140° at the after cross-section. For OEEVM+WM and LDKM the agreement with the experimental data is reasonable (within 15%), whereas for OEEVM the primary vortices are too far away from the body surface, but at the correct angle. This is related to the incorrect boundary layer profiles and hull-pressure distributions attributed to the OEEVM.

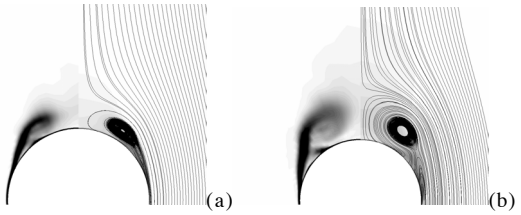

Figure 12. Secondary streamlines superimposed on contours of k (left) and on U (right) for the OEEVM. (a) α=20° and x/L=0.6, (b) α=20° and x/L=0.772.

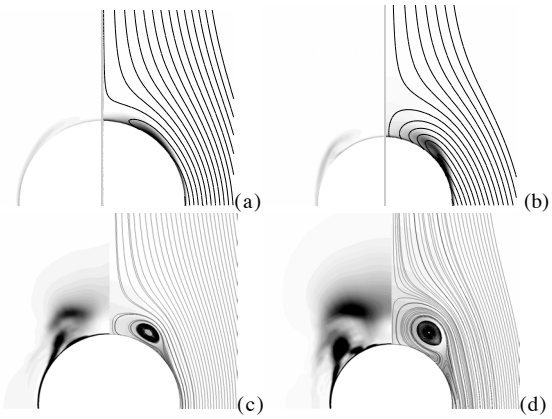

Figure 13. Secondary streamlines superimposed on contours of k (left) and on U (right) for the LDKM. (a) α=10° and x/L=0.6, (b) α=10° and x/L=0.772, (c) α=20° and x/L=0.6, and (d) α=20° and x/L=0.772.

10. Summary and Outlook

When LES is used to study 'building-block' flows for which the method originally was invented, it produces excellent results. The dependency of the results on the subgrid model is weak – almost all subgrid models produce identical results. For free-flows (e.g. jets and mixing layers) good agreement is usually obtained even for very high Re-number flows. For high Re-number wall-bounded flows, LES becomes more involved as the scales become smaller and smaller as the wall is approached. As the Re-number increases we cannot afford resolving all scales even if local grid refinement or adaptive meshes are used. This puts additional demands on the subgrid model, which may be combined with a separate wall-modell, as frequently done in RANS. Here we have tried to highlight this problem and to present an overview of methods that currently are available.

The results presented suggest that the dynamic approach, in which the model coefficients are determined from the smallest resolved scales, can produce accurate predictions even on moderately fine grids, thus allowing high Re-number flows to be investigated. The explanation for this appears to be that the eddy-viscosity responds to the accumulation of energy in the small scales by adjusting the dissipation before it contaminates the resolved scales, although the sub-

grid stress-tensor is not generally alined with the rate-of-strain tensor. Structural models are theoretically better suited for complex anisotropic flows but are not always numerically stable, unless a fine grid can be used. MILES, on the other hand, provides an interesting alternative, being related to both structural and functional models, but is associated with the advantage/drawback of its strong coupling with the numerical schemes used. Wall-models provides an attractive alternative, but appears to be sensitive to the flow conditions, and is not allowed to deviate too much from the flat plate boundary layer for which they are developed. For the future the TLS method and the homogenization-based LES models may provide very interesting alternatives.

Acknowledgments

Some of the presented computations were preformed with an earlier research version of the FOAM™ code, for further details see http://www.nabla.com.uk

References

[1] Speziale C.G.; 1996, "Modeling of Turbulent Transport Equations", in Simulation and Modeling of Turbulent Flows Eds. Gatski T.B., Hussaini M.Y. & Lumeley J.L. Oxford University Press, New York.

[2] Launder B.E.; 1996, "An Introduction to Single-Point Closure Methodology", in Simulation and Modeling of Turbulent Flows Eds. Gatski T.B., Hussaini M.Y. & Lumeley J.L. Oxford University Press, New York.

[3] Wilcox D.C.; 1998, "Turbulence Modelling for CFD", DCW Industries.

[4] Pope S.B.; 2000, "Turbulent Flows", Cambridge University Press.

[5] Ferziger J.H. & Leslie D.C.; 1979, "Large Eddy Simulation – A Predictive Approach to Turbulent Flow Computation", AIAA paper 79-1441.

[6] Sagaut, P.: Large Eddy Simulation for Incompressible Flows, Springer Verlag, Heidelberg, 2001.

[7] Fureby C.; 2001, "Towards Large Eddy Simulation of Complex Flows, In Direct and Large Eddy Simulation IV, Eds. Friedrich R. & Rodi W., Kluwer, The Netherlands.

[8] Lesieur M & Metais O; 1996, "New Trends in Large Eddy Simulations of Turbulence", Annu. Rev. Fluid Mech., **28**, p 45.

[9] Boris, J.P., Grinstein, F.F., Oran, E.S. & Kolbe, R.L.; 1992, "New Insights into Large Eddy Simulation", Fluid Dyn. Res., **10**, p 199.

[10] Grinstein F.F. & Karniadakis G.E.; 2002, "Special Section on Alternative LES and Hybrid RANS/LES for Turbulent Flows", J. Fluids Eng., **124**, p 821.

[11] Bagget J.S., Jiménez J. & Kravchenko A.G.; 1997, "Resolution Requirements in Large Eddy Simulations of Shear Flows", Ann. Res. Breiefs, CTR, NASA Ames/Stanford University, p 55.

[12] Ghosal, S. & Moin P.; 1995, "The Basic Equations for the Large Eddy Simulation of Turbulent Flows in Complex Geometry", J. Comp. Phys., **118**, p 24.

[13] Fureby, C. & Tabor, G.; 1997, "Mathematical and Physical Constraints on Large Eddy Simulations", J. Theoretical Fluid Dyn., **9**, 85.

[14] Vreman B., Geurts B. & Kuerten H.; 1994, "Realizability Conditions for the Turbulent Stress Tensor in Large Eddy Simulation", J. Fluid Mech., **278**, p 351.

[15] Speziale C.G.; 1985, "Galilean Invariance of Sub Grid Scale Stress Models in the Large Eddy Simulation of Turbulence", J. Fluid Mech., **156**, p 55.

[16] Geurts B.J.; 2001, "Balancing Errors in LES", In Direct and Large Eddy Simulation IV, Eds. Friedrich R. & Rodi W., Kluwer, The Netherlands.

[17] Schumann U.; 1975, "Subgrid Scale Model for Finite Difference Simulation of Turbulent Flows in Plane Channels and Annuli", J. Comp. Phys., **18**, p 376.

[18] Smagorinsky J.; 1963, "General Circulation Experiments with the Primitive Equations. I. The Basic Experiment", Month. Wea. Rev., **91**, p 91.

[19] Germano M., Piomelli U., Moin P. & Cabot W.H.; 1994, "A Dynamic Sub Grid Scale Eddy Viscosity Model", Phys. Fluids A **3**, p 1760.

[20] Ghosal S., Lund T.S., Moin P. & Akselvoll K.; 1995, "A Dynamic Localization Model for Large Eddy Simulation of Turbulent Flows", J. Fluid Mech, **286**, p 229.

[21] Kim W.-W. & Menon S.; 1994, "A New Dynamic One Equation Sub Grid Scale Model for Large Eddy Simulations", AIAA Paper No 95-0356.

[22] Kim W.-W. & Menon S.; 1997, "Application of the Localized Dynamic Subgrid Scale Model to Turbulent Wall-Bounded Flows", AIAA Paper No 97-0210.

[23] Kim W.-W., & Menon S.; 1999, "A new Incompressible Solver for Large-Eddy Simulations", Int. J. Num. Fluid Mech., **31**, p 983.

[24] Meneveau C., Lund T.S. & Moin P.; 1996, "A Lagrangian Dynamic Subgrid-scale Model of Turbulence", J. Fluid Mech., **319**, p 353.

[25] Bardina J., Ferziger J.H. & Reynolds W.C.; 1980, "Improved Subgrid Scale Models for Large Eddy Simulations", AIAA Paper No. 80-1357.

[26] Deardorff, J.W.; 1973, "The Use of Subgrid Transport Equations in a Three-Dimensional Model of Atmospherical Turbulence", ASME, J. Fluids Engng. Trans., **95**, 429.

[27] Carati D. & Cabot W.; 1996, "Anisotropic Eddy Viscosity Models", Proceedings of the Summer Program – CTR, p 325.

[28] Abba A., Bucci R., Cercignani C. & Valdettaro L.; 1996, "A New Approach to the Dynamic Subgrid Scale Model", Unpublished.
[29] Horiuti K.; 1993, "A Proper Velocity Scale for Modelling Subgrid Scale Eddy Viscosities in Large Eddy Simulation", Phys. Fluids A, **5**, p 146.
[30] Sullivan P.P., McWilliams J.C. & Moeng C.H.; 1994, "A Subgrid Scale Model for Large Eddy Simulation of Planetary Boundary Layer Flows", Boundary-layer Meteorol., **71**, p 247.
[31] Voke, P.; 1996, "Subgrid-scale Modeling at Low Mesh Reynolds Number", J. Theoretical Fluid Dyn., **8**, p 131.
[32] Wang M.; 1997, "Progress in Large Eddy Simulation of Trailing Edge Turbulence and Aeroacoustics", Annual Research Briefs – CTR, p 37.
[33] Wang M. & Moin P.; 2001, "Wall Modelling in LES of Trailing Edge Flow", Turbulence and Shear Flow Phenomena, Vol II, Eds. Lindborg E. *et al.*, p 165.
[34] Spalart P.R. & Allmaras S.R.; 1992, "A One-Equation Turbulence Model for Aerodynamic Flows", AIAA 92-0439.
[35] Spalart P.R., Jou W.-H., Strelets M. & Allmaras S.R.; 1997, "Comments on the Feasibility of LES for wings, and on a Hybrid RANS/LES Approach", Advances in DNS/LES, 1st AFSOR Int. Conf. On DNS/LES, Greyden Press, Columbus Oh.
[36] Nikitin N.V., Nicoud F., Wasistho B., Squires K. D. & Spalart P.R.; 2000, "An Approach to Wall Modelling in Large Eddy Simulations", Phys. Fluids, **12**, p 1629.
[37] Boris J.P. & Book D.L.; 1973, "Flux Corrected Transport I, SHASTA, a Fluid Transport Algorithm that Works", J. Comp. Phys. **11**, p 38.
[38] Garnier E., Mossi M., Sagaut P., Comte P., & Deville M.; 2000, "On the Use of Shock-Capturing Schemes for Large Eddy Simulation", J. Comp. Phys., **153**, p. 273.
[39] Okong'o N., Knight D.D., & Zhou G.; 2000, "Large Eddy Simulations Using an Unstructured Grid Compressible Navier-Stokes Algorithm", Int. J. Comp. Fluid Dynamics **13**, p. 303.
[40] Margolin L.G., Smolarkiewicz P.K., & Sorbjan Z.; 1999, "Large-Eddy Simulation of Convective Boundary Layers Using Non-Oscillatory Differencing", Physica D, **133**, p 390.
[41] Karamanos G.-S. & Karniadakis G.E.; 2000, "A Spectral Vanishing Viscosity Method for Large-Eddy Simulations", J. Comp. Phys., **163**, p 22.
[42] Fureby C. & Grinstein F.F.; 2002 "Large Eddy Simulation of High Reynolds Number Free and Wall Bounded Flows", J. Comp. Phys., **181**, p 68.
[43] Grinstein F.F. & Fureby C.; 2002, "Recent Progress on MILES for High Re Flows", J. Fluids Engng., **124**, p 848.
[44] Kemenov K. & Menon S.; 2002, "TLS: A New Two Level Simulation Methodology for High-Reynolds LES", AIAA Paper No 2002-0287.
[45] Kemenov K. & Menon S.; 2002, "A Two-Level Simulation Methodology for LES of High Reynolds Number Flows", Advances in Turbulence IX, Eds. Castro *et al.*, p 203, CIMNE Press.
[46] Kerstein A.; 1999, "One-dimensional Turbulence: Model formulation and application to Homogeneous Turbulence, Shear Flows and Buyoant Stratified Flows", J. Fluid Mech., **392**, p 277.
[47] Persson L., Fureby C. & Svanstedt N.; 2002, "On Homogenisation based Methods for Large Eddy Simulation", J. Fluids Engng., **124**, p 892.
[48] Bensoussan A., Lions J.L. & Papanicolaou G.; 1978, Asymptotic Analysis for Periodic Structures, North-Holland.
[49] Hirsch C.; 1999, "Numerical Computation of Internal and External Flows", J. Wiley & Sones.
[50] Sandham N.D. & Howard R.J.A.; 1995, "Statistics Databases from Direct Numerical Simulation of Fully-Developed Turbulent Channel Flow", Private communication, QMW-EP-1106, Queen Mary & Westfield College, Department of Engineering. London, UK.
[51] Antonia R.A., Teitel M., Kim J., & Browne L.W.B.; 1992, "Low-Reynolds-Number Effects in a Fully Developed Turbulent Channel Flow", J. Fluid Mech. **236**, p 579.
[52] Wei T. & Willmarth W.W.; 1989, "Reynolds Number Effects on the Structure of a Turbulent Channel Flow", J. Fluid Mech. **204**, p 57.
[53] Dean R.B.; 1978, "Reynolds Number Dependence of Skin Friction and other Bulk Flow Variables in Two-Dimensional Rectangular Duct Flow", Trans. ASME I: J. Fluids Eng., **100**, p 215.
[54] Patel N., Stone C. & Menon S.; 2003, "Large Eddy Simulation of Turbulent Flow over an Axisymmetric Hill", AIAA Paper 03-0967.
[55] Simpson R., Long C., & Byun G.; 2002, "Study of Vortical Separation from an Axisymmetric Hill", Int. J. of Heat and Fluid Flow, To Appear.
[56] Simpson R.; 2001, "Structure of Rough-wall Three-dimensional Turbulent Boundary Layers and Vortical Separations" Turbulence and Wakes Program Review, Office of Naval Research.
[57] Hedin, P.-O., Alin, N., Berglund, M. & Fureby, C.: 2001, "Large Eddy Simulation of the Flow Around an Inclined Prolate Spheroid", AIAA Paper 01-1035.
[58] Wikström N., Svennberg U. Alin N. & Fureby C.; 2002, "LES of the Flow Past an Inclined Prolate Spheroid", In preparation for AIAA.J.
[59] Barber K.M. & Simpson R.L.; 1991, "Mean Velocity and Turbulence Measurements of Flow

Around a 6:1 Prolate Spheroid", AIAA Paper 91-0255.
[60] Ahn S. & Simpson R.L.; 1992, "Cross-Flow separation on a Prolate Spheroid at Angles of Attack", AIAA Paper 92-0428.
[61] Chesnakas C.J. & Simpson R.L.; 1996, "Measurements of Turbulence Structure in the Vicinity of a 3D Separation", J. Fluids Eng., **118**, p 268.
[62] Chesnakas, C.J. & Simpson, R.L.; 1996, "Measurements of Turbulence Structure in the Vicinity of a 3D Separation", J. Fluids Eng., **118**, p 268.
[63] Wetzel T.G., Simpson R.L. & Chesnakas C.J.; 1998, "Measurement of Three-Dimensional Crossflow Separation", AIAA.J. **36**, p 557.
[64] Goody M., Simpson R.L. & Engel M.; 1998, "Mean Velocity and Pressure and Velocity Spectral Measurements within a Separated Flow Around a Prolate Spheroid at Incidence", AIAA Paper 98-0630.
[65] Simpson R.L.; 2000, "Steady Flow over a 6:1 Prolate Spheroid", www.aoe.vt.edu/aoe/prolatespheroid. also at J. Fluids Engng. databank.
[66] Han T. & Patel V.C.; 1979, "Flow Separation on a Spheroid at Incidence", J. Fluid Mech. **92**, p 643.
[67] Constantinescu G.S., Pasinato H., Wang Y.-Q., Forsythe J.R. & Squires K.D.; 2002, "Numerical Investigation of Flow past a Prolate Spheroid", AIAA 02-0588.